Journal of Alloys and Compounds 724 (2017) 684–694

Contents lists available at ScienceDirect

Journal of Alloys and Compounds

journal homepage: http://www.elsevier.com/locate/jalcom

Simple, ultra-rapid, versatile method to synthesize cobalt/cobalt oxide nanostructures on carbon fiber paper via intense pulsed white light (IPWL) photothermal reduction for energy storage applications

Sanghyun Lee [a], Sung-Hyeon Park [b], Kihun Jang [a], Seongil Yu [a], Chiho Song [a], Hak-Sung Kim [b, c, **], Heejoon Ahn [a, c, *]

[a] Department of Organic and Nano Engineering, Hanyang University, 17 Haengdang-dong, Seongdong-gu, Seoul 04763, South Korea
[b] Department of Mechanical Engineering, Hanyang University, 17 Haengdang-dong, Seongdong-gu, Seoul 04763, South Korea
[c] Institute of Nano Science and Technology, Hanyang University, 17 Haengdang-dong, Seongdong-gu, Seoul 04763, South Korea

ARTICLE INFO

Article history:
Received 5 December 2016
Accepted 7 July 2017
Available online 8 July 2017

Keywords:
Intense pulsed white light
Photothermal reduction
Nanostructure
Energy storage
Cobalt oxide

ABSTRACT

Cobalt-based nanomaterials have received considerable attention in electric energy-storage devices due to their outstanding electrochemical characteristics. However, multiple time- and energy-consuming steps and complex reduction processes for producing cobalt and cobalt oxide nanostructures are disrupting their substantive commercialization. Here, we propose a facile, ultra-fast, and versatile method for the fabrication of cobalt and cobalt oxide nanostructures using an intense pulsed white light (IPWL) photothermal reduction technique. The mechanism of the IPWL photothermal reduction of cobalt and cobalt oxide is firstly studied by measuring the in-situ temperature of the $Co(NO_3)_2$-coated carbon fiber paper (CFP) substrate during IPWL irradiation and analyzing the crystal structures of the IPWL-irradiated samples. Cobalt nanoflakes and cobalt oxide nanoparticles are synthesized on the surface of the CFP substrate by irradiating IPWL for 10 ms at ambient temperature and pressure with various energy densities from 10 to 30 J cm^{-2}. The Co_3O_4 nanoparticle/CFP and Co nanoflake/CFP samples are further utilized as an electrode, and each electrode exhibits high specific capacity of 29 and 73 mA h g^{-1}, respectively, at a current density of 1 A g^{-1}. Since this novel photothermal reduction technique is applicable to other transition metals and metal oxides, it is a promising method for not only energy storage systems, but also for energy generation applications, filters, sensors, and catalysis systems.

1. Introduction

Transition elements are a group of elements occupying the middle portion of the periodic table between the main group elements. The transition elements are all metals and are therefore known as transition metals. Among them, cobalt is one of the most attractive materials because of its excellent ferromagnetic, catalytic, electronic, and photonic properties [1]. Also, cobalt exhibits superb heat, corrosion, and wear resistance when it is alloyed with other metals [2]. Due to these properties, cobalt-based materials are used in various fields such as Li-ion batteries, supercapacitors, catalysts, magnetic data storage, pigments, and hard metal alloys [3–9]. A variety of methods for obtaining high-purity metallic cobalt and cobalt oxide have been investigated for a long time since the discovery of cobalt in 1735. In general, metallic cobalt can be obtained by reduction of cobalt oxide. The carbothermal reduction method, in which cobalt is calcined with carbon in a blast furnace hotter than 1000 °C, is commonly used in industrial fields, but it requires a very high thermal energy and large-scale facilities [10]. Several other methods have also been developed in the laboratory to reduce cobalt oxide, including flame spray reduction, polyol processes, thermal decomposition of organic salts, solution phase chemical reduction of metal salts, supercritical hydrothermal synthesis, freeze-drying, and hydrogen reductions [11–17]. However, these methods require complex multiple processes, a high temperature treatment, and a long reaction time. In addition, high-cost facilities are needed because these reduction processes usually occur in an inert gas atmosphere such as N_2 or Ar. For this reason, it

* Corresponding author. Department of Organic and Nano Engineering, Hanyang University, 17 Haengdang-dong, Seongdong-gu, Seoul 04763, South Korea.
** Corresponding author. Department of Mechanical Engineering, Hanyang University, 17 Haengdang-dong, Seongdong-gu, Seoul 04763, South Korea.
E-mail addresses: kima@hanyang.ac.kr (H.-S. Kim), ahn@hanyang.ac.kr (H. Ahn).

http://dx.doi.org/10.1016/j.jallcom.2017.07.069
0925-8388/

is significant to develop simple, rapid, and facile routes for the formation of cobalt (or the reduction of cobalt oxide).

With the development of nanomaterials, it is well recognized that tailoring the size and shape of the nanomaterial is key to enhancing various properties such as electric, magnetic, catalytic, and electrochemical. In electrode applications, designing and constructing the hierarchical porous structure is crucial because the porosity, pore size, and homogeneity of the porous materials could enhance the specific capacity, ionic diffusion, and rate capability of the electrodes by offering large numbers of chemically active sites, shortening the ion transport pathways, and providing an abundant pore volume to store electrolytes. As a result, considerable effort has been devoted to building a variety of nanostructures of cobalt, including nanoparticles, nanorods, nanowires, nanodisks, nanocapsules, nanobelts and nanobowls [18–29]. However, only a few reports are available on the fabrication of nanoflake structures of cobalt [30,31]. Yang et al. studied the fabrication of cobalt nanoflakes using the hydrothermal reduction of a cobalt organic compound, and Senapati et al. used Ag-catalyst to synthesize hierarchical cobalt nanoflowers at a low reduction temperature less than 100 °C [32,33]. However, environmental problems and the low purity of cobalt remain because many additives, such as reducing agents, catalysts, and capping agents, are used for easy reduction of cobalt oxide at low temperatures.

Motivated by these issues, we report a simple, ultra-rapid, and versatile method to synthesize cobalt/cobalt oxide nanostructures using intense pulsed white light (IPWL) photothermal reduction at ambient temperature and pressure. A high intensity pulsed white light is generated from a xenon lamp emitting a light spectrum in the visible region through arc plasma generation [34]. Recently, the IPWL technique has attracted considerable attention because of its ultrafast and low temperature sintering capability and layer selectivity, which is suitable for large-area printed electronics [35–37]. In contrast to the conventional thermal sintering technique, in which samples have to be exposed to a high temperature for a long reaction time, IPWL irradiation transfers the required heat energy in the form of light within a few milliseconds. In addition, metal nanoparticles can be annealed by IPWL irradiation without damaging the underlying substrates, such as glass or flexible polymers, which are sensitive to high temperatures. The overall process of IPWL is conducted over a short time in an air atmosphere and it is more economic than conventional sintering methods. In this report, cobalt and cobalt oxide nanostructures were fabricated on a carbon fiber paper (CFP) substrate by irradiating IPWL directly on the $Co(NO_3)_2$-coated CFP substrate (Fig. 1). To understand the reduction mechanism of cobalt and cobalt oxide on the CFP substrate by IPWL irradiation, the correlation of the IPWL irradiation energy was analyzed with the morphology and oxidation states of cobalt by measuring the temperature of the samples at various IPWL irradiation energies of 10–30 J cm^{-2}. The synthesized cobalt and cobalt oxide nanostructures on the CFP substrates were further utilized for energy storage applications.

2. Experimental

2.1. Fabrication of Co and Co-oxide on carbon fiber paper by IPWL irradiation

The IPWL irradiating system consists of a xenon flash lamp (PerkinElmer Co.), a power supply, capacitors, a simmer triggering controller, a pulse controller, and a water-cooling system. The IPWL from the xenon flash lamp has a broad wavelength range from 350 to 1000 nm. The system is designed to supply a maximum of 99 shots and 100 J cm^{-2} energy in a millisecond scale, with a minimum pulse interval of 1 ms, by controlling the electrical current and voltage. For the fabrication of Co and Co-oxide on carbon fiber paper (CFP), a CFP (Spectracarb-2050L) substrate with a thickness of 0.2 mm was cleaned in DI water and dried in an oven. Both sides of the CFP were treated by a UV/ozone cleaner (YUILUV, YUC-030602) for 5 s each. The CFP substrate was then immersed in an aqueous cobalt precursor solution of 1 M $Co(NO_3)_2 \cdot 6H_2O$ for 30 min and dried at 40 °C for 2 h in an oven. In order to measure the temperature of the sample during IPWL irradiation, a thermocouple (HH-K-24-SLE-500, Type-K, 0.24 mm, OMEGA Co.) was attached to the CFP using silver paste as shown in Fig. 2. The $Co(NO_3)_2 \cdot 6H_2O$ precursor coated CFP samples were placed at a distance of 3 mm from the IPWL lamp and the light was irradiated for 10 ms with various energies from 10 to 30 J cm^{-2}. The energy of the irradiated IPWL was measured by a power meter (Nova II, People Laser Tech.). The IPWL irradiated sample was rinsed with DI water to remove the unreacted metal oxide precursor and dried in an oven.

2.2. Structure characterization

The crystal structures of the fabricated samples were analyzed using X-ray diffraction (XRD, RIGAKU D/MAX2500V) with monochromatized Cu-Kα radiation. The surface morphology and microstructure of the samples were investigated by a field-emission scanning electron microscope (FESEM, Hitachi S-4800). The Brunauer-Emmett-Teller (BET) surface area of the samples was determined using an automatic physisorption analyzer (3-FLEX, Micromeritics) at 77 K. Prior to BET measurements, the samples were degassed at 250 °C for 6 h in a vacuum condition. Pore-size distributions were calculated by the Barrett-Joyner-Halenda (BJH) method using the adsorption branch of the isotherm.

2.3. In-situ temperature measurement

The temperature measurement system was devised combining a non-inverting amplifier circuit with an op-amp (LM 324N, STMicroelectronics), a power supply (SDP 30-3DT, SM Techno) and a type-K thermocouple with a response time of approximately 1 ms. The power supply was used to apply a constant voltage (15 V) to the non-inverting amplifier circuit for operating the op-amp. In the non-inverting amplifier circuit, the values of the resistances R_1 and R_3 were fixed at 10 kΩ, while R_2 and R_4 were fixed at 100 kΩ. During irradiation, the output voltage (V_{out}) was recorded using an oscilloscope (DL1740E; Yokogawa) at 20 × 10^4 samples per second. Based on the non-inverting amplifier circuit, the temperature changes of the silver paste during irradiation were calculated from the output voltage (V_{out}) using the following equations [38]:

$$V_{out} = V_{in} \times [(1 + R_2/R_1) \times (1 + R_4/R_3)] \quad (1)$$

$$V_{in} = \Delta T_{measured}/\alpha \quad (2)$$

$$\Delta T_{measured} = V_{out} \times \alpha / [(1 + R_2/R_1) \times (1 + R_4/R_3)] \quad (3)$$

where V_{out} is the output voltage recorded by the oscilloscope, V_{in} is the voltage differential converted by the temperature gradient of the silver paste, $\Delta T_{measured}$ is the temperature change of the silver paste, and α is a correction factor, which was measured as 0.025 °C V^{-1}.

2.4. Transient heat transfer analysis

Transient heat transfer analysis was conducted to calculate the CFP temperature. As shown in Fig. 2, the modeled heat transfer

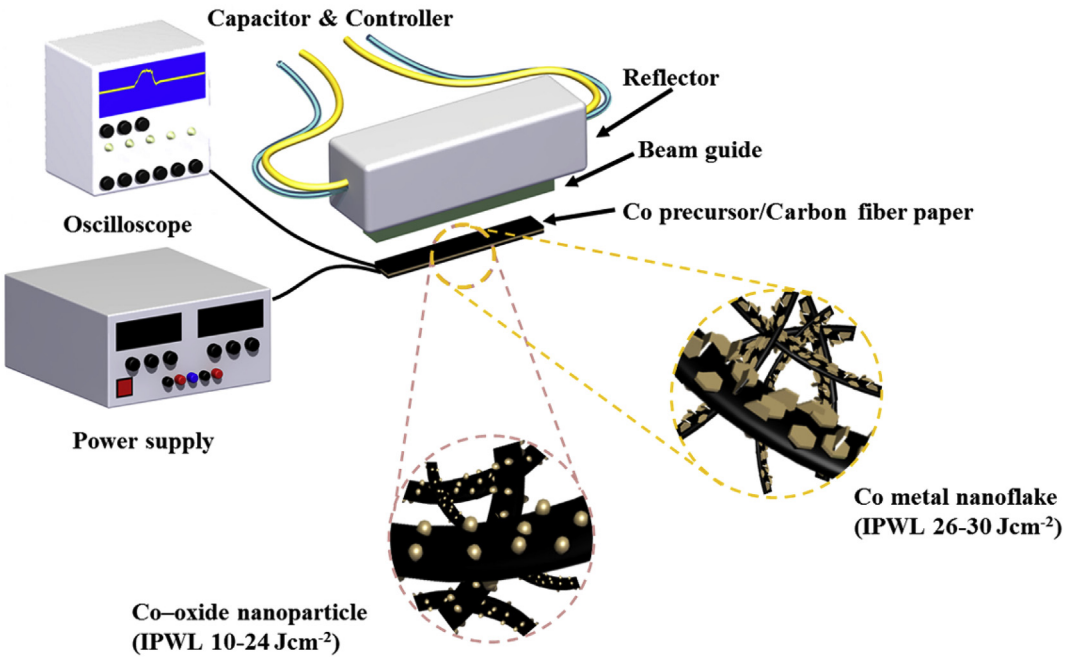

Fig. 1. Schematics of the IPWL radiation process for the synthesis of Co metal nanoflakes and Co-oxide nanoparticles on CFP.

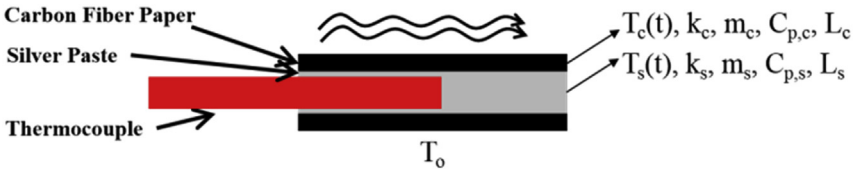

Fig. 2. Theoretical heat transfer model for calculation of the temperature of the CFP.

system was composed of the CFP, silver paste, and the floor. Several assumptions were employed to calculate the temperature changes in this model. First, radiation of heat from the CFP was neglected. Second, convection between the air surroundings and the CFP was assumed to occur through a mechanism of natural convection. Third, for simplicity, the values of the thermal properties of CFP, and silver paste were fixed at their specific values at room temperature, as listed in Table 1. The general heat transfer equation can be written as follows:

$$q_{o,c} = h(T_c(t) - T_\infty) + k_c(T_c(t) - T_s(t))/L_c + m_c C_{p,c}(dT_c(t)/dt) \quad (4)$$

Table 1
Physical constants of CFP and silver paste.

	Carbon	Silver paste
Specific gravity, ρ (kg/m^3)	2260	10400
Thermal conductivity, k (W/m· °C)	150	429
Heat capacity in the solid phase, $C_{p,s}$ (J/kg· °C)	709.75	235
Latent heat of fusion (J/kg)	–	88.0
Bulk melting temperature, T_m (°C)	–	961.78
Density (g/cm^3)	2.267	10.49
Thickness, L (um)	200	–
Mass, m (g)	0.2267	9.074

$$q_{o,s} = k_s(T_s(t) - T_o)/L_s + k_c(T_s(t) - T_t(t))/L_c + m_s C_{p,s}(dT_s(t)/dt) \quad (5)$$

where q_o is the heat flux that is assumed to be an average of the IPWL energy divided by the pulse duration, T is the temperature, h is the natural convection coefficient, k is the thermal conductivity, L is the thickness, m is the mass, C_p is the heat capacity, and h is the natural convection coefficient (30 W m^{-2}K^{-1}). The subscripts c and s denote the CFP and silver paste, respectively. Equations (4) and (5) can be rearranged to produce $T_c(t)$ and $T_s(t)$:

$$dT_c(t)/dt = (cT_c(t) + dT_s(t) + e)/\alpha \quad (6)$$

$$dT_s(t)/dt = (dT_c(t) + fT_s(t) + g)/\beta \quad (7)$$

where $\alpha = m_c \cdot C_{p,c}$, $\beta = m_s \cdot C_{p,s}$, $c = -(k_c/L_c + h)$, $d = k_c/L_c$, $e = q_{o,c} + h \cdot T_0$, $f = k_c/L_c + K_s/L_s$ and $g = q_{o,s} + (k_s/L_s)T_0$.

For the heat transfer calculations, the following initial conditions were assumed:

$$T_c(0) = T_\infty, T_s(0) = T_0, q_{o,s} = 0 \quad (8)$$

To solve the temperatures of the CFP and silver paste, the eigenvalues technique was employed, thereby obtaining the following homogeneous and particular solutions:

$$T_{h,c}(t) = C_1 \cdot d \cdot e^{\lambda_1 t} + C_2 \cdot d \cdot e^{\lambda_2 t} \quad (9\text{-a})$$

$$T_{h,s}(t) = C_1 \cdot (-c + \lambda_1 \alpha) \cdot e^{\lambda_1 t} + C_2 \cdot (-c + \lambda_2 \alpha) \cdot e^{\lambda_2 t} \quad (9\text{-b})$$

$$T_{p,c}(t) = (dg - ef) \Big/ \left(cf - d^2\right) \quad (10\text{-a})$$

$$T_{p,s}(t) = (de - cg) \Big/ \left(cf - d^2\right) \quad (10\text{-b})$$

where $T_{h,c}$ and $T_{h,s}$ are the homogeneous solutions for the temperatures of the CFP and the silver paste, respectively; $T_{p,c}$ and $T_{p,s}$ are the particular solutions for the temperatures of the CFP and substrate, respectively. The temperatures of the CFP and silver paste were determined using the following combination of homogeneous and particular solutions:

$$\begin{aligned} T_c(t) &= T_{h,c}(t) + T_{p,c}(t) \\ &= C_1 \cdot d \cdot e^{\lambda_1 t} + C_2 \cdot d \cdot e^{\lambda_2 t} + (dg - ef) \Big/ \left(cf - d^2\right) \end{aligned} \quad (11\text{-a})$$

$$\begin{aligned} T_s(t) &= T_{h,s}(t) + T_{p,s}(t) \\ &= C_1 \cdot (-c + \lambda_1 \alpha) \cdot e^{\lambda 1 t} + C_2 \cdot (-c + \lambda_2 \alpha) \cdot e^{\lambda 2 t} \\ &\quad + (de - cg) \Big/ \left(cf - d^2\right) \end{aligned} \quad (11\text{-b})$$

where

$$\lambda_1 = \left[(\alpha f + \beta c) + \sqrt{(\alpha f - \beta c)^2 + 4\alpha\beta d^2}\right] \Big/ 2\alpha\beta \quad (12\text{-a})$$

$$\lambda_2 = \left[(\alpha f + \beta c) - \sqrt{(\alpha f - \beta c)^2 + 4\alpha\beta d^2}\right] \Big/ 2\alpha\beta \quad (12\text{-b})$$

$$\begin{aligned} C_1 = \Big[T_0 - \Big\{T_\infty - (dg - fe) \Big/ \left(cf - d^2\right)\Big\}(-c + \lambda_2\alpha)/d - (de \\ - cg) \Big/ \left(cf - d^2\right)\Big] \Big/ \alpha(\lambda_1 - \lambda_2) \end{aligned} \quad (13\text{-a})$$

$$\begin{aligned} C_2 = \Big[T_\infty - (dg - fe) \Big/ \left(cf - d^2\right)\Big] \Big/ d - \Big[T_0 - \Big\{T_\infty - (dg - fe) \Big/ \left(cf \\ - d^2\right)\Big\}(-c + \lambda_2\alpha)/d - (de - cg) \Big/ \left(cf - d^2\right)\Big] \Big/ \alpha(\lambda_1 - \lambda_2) \end{aligned} \quad (13\text{-b})$$

2.5. Electrochemical characterization

All electrochemical measurements were conducted as three-electrode configurations using a CHI 660D electrochemical workstation (CH instrument, USA) in a 2 M KOH solution. For the three-electrode configuration, the Co or Co-oxide/CFP sample acted as the working electrode. Hg/HgO served as the reference electrode and a platinum coil was used as the counter electrode. The electrochemical properties of the Co or Co-oxide/CFP electrodes were studied by cyclic voltammetry (CV) and galvanostatic charge-discharge (CD) measurements. The specific capacity was calculated from CV and CD curves, and the cycle stability was performed at a scan rate of 50 mV s^{-1} for up to 5000 cycles.

3. Results and discussion

3.1. Structural and morphological studies

The crystallinity and morphology of the samples synthesized at different energy densities by IPWL irradiation were analyzed using an X-ray diffraction (XRD) and field-emission scanning electron microscope (FE-SEM). Fig. 3 shows the XRD spectra of the samples irradiated at various energy densities (10–30 J cm^{-2}) of IPWL. In the case of IPWL irradiation of the Co precursor with low energy densities (10–18 J cm^{-2}), peaks appeared at 31.3, 36.9, 44.8, 59.4, and 65.3°, corresponding to the (220), (311), (400), (511), and (440) planes of Co_3O_4 (JCPDS #76-1802), respectively. As the energy density increased from 18 to 24 J cm^{-2}, the Co_3O_4 peaks disappeared and new peaks appeared at 36.4, 42.3, 61.4, 73.6, and 77.5°, assignable to the (111), (200), (220), (311), and (222) planes of CoO (JCPDS #78-0421). Note that the Co peaks were also observed at 44.2, 51.5, and 76.8°, corresponding to the (111), (200), and (220) planes of Co metal (JCPDS #74-1057), respectively. At high energy densities greater than 26 J cm^{-2}, the CoO peaks completely disappear and the cobalt metal peaks become apparent. The XRD patterns of metallic cobalt indicate the specific crystal structure of a face-centered-cubic (β-cobalt), which is commonly obtained when cobalt oxide is reduced using hydrogen gas at temperatures greater than 450 °C [39]. As a result of the XRD experiment shown in Fig. 3, Co_3O_4 can be reduced from the Co precursor by IPWL irradiation with an energy density less than 18 J cm^{-2}, and metallic cobalt can be obtained at an energy density greater than 26 J cm^{-2}. At intermediate energy densities of 20–24 J cm^{-2}, a mixture of Co_3O_4, CoO, and Co metal was obtained.

Fig. 4 shows the FE-SEM images of the surface of $Co(NO_3)_2$-coated CFP irradiated by IPWL at various energy densities from 10 to 30 J cm^{-2}. Pristine CFP, which was used as a substrate, is

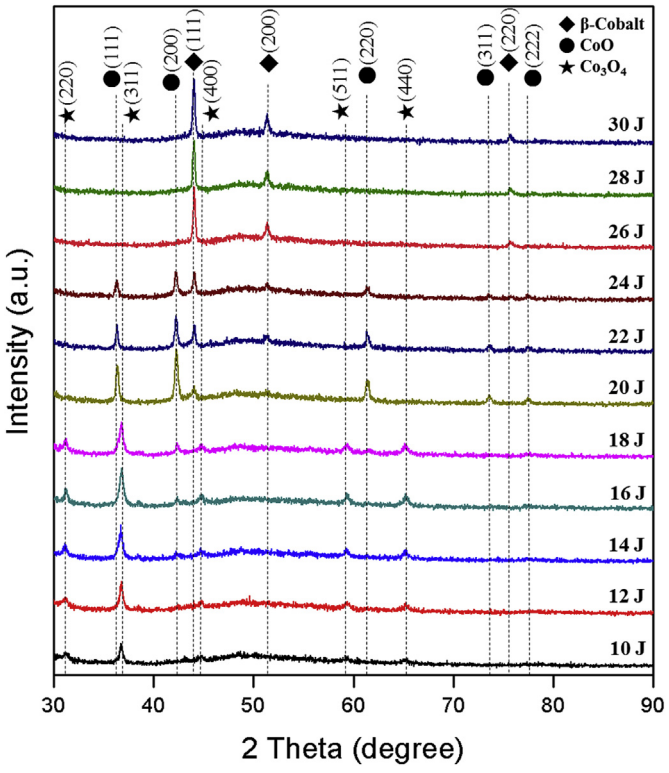

Fig. 3. XRD spectra of the $Co(NO_3)_2$-coated CFP substrates after IPWL irradiation with various energy densities.

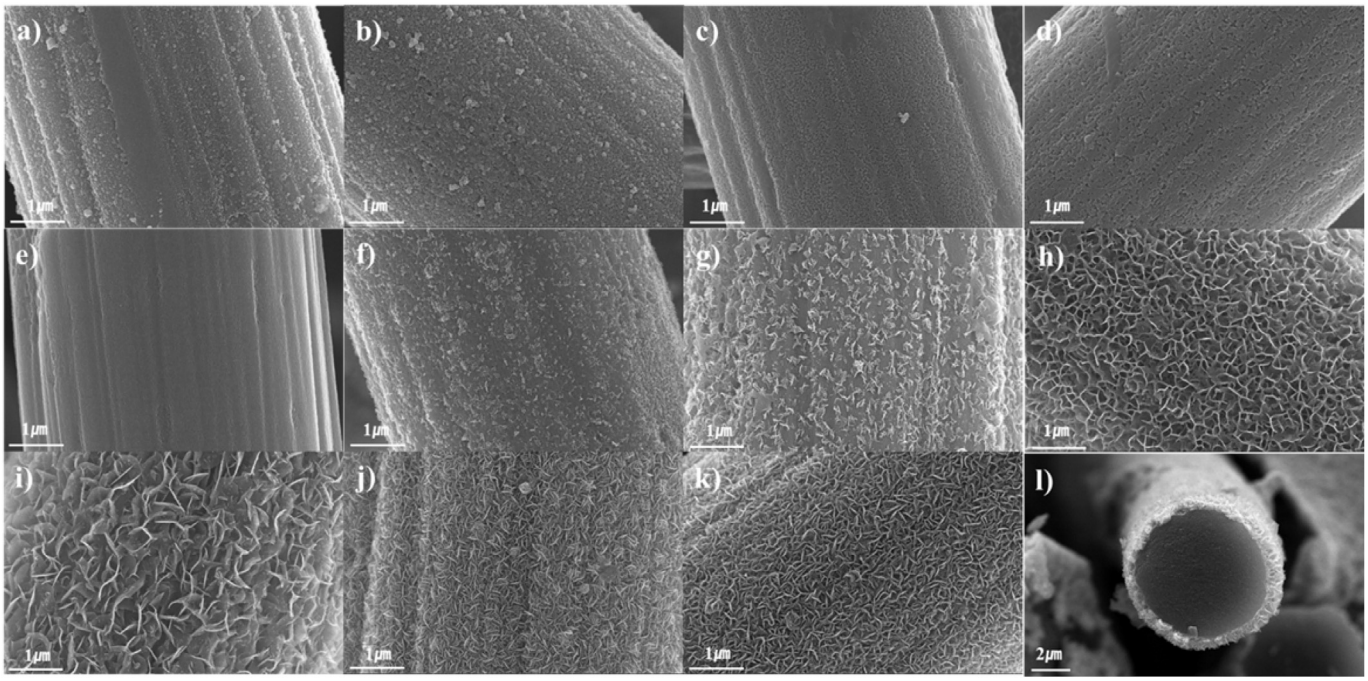

Fig. 4. FE-SEM images of the $Co(NO_3)_2$-coated CFP substrates after IPWL irradiation with (a) 10, (b) 12, (c) 14, (d) 16, (e) 18, (f) 20, (g) 22, (h) 24, (i) 26, (j) 28 and (k) 30 J cm^{-2}. (l) Cross-sectional SEM image of the $Co(NO_3)_2$-coated carbon fiber after IPWL irradiation with 30 J cm^{-2}.

composed of carbon fibers with an average diameter of approximately 6–8 μm. As shown in Fig. 4a–e, nano-sized particles (approximately 10–100 nm) were deposited on the surface of CFP after IPWL irradiation of 10–18 J cm^{-2}. The number of particles gradually increased with an increase in the energy density of IPWL, while the particle size decreased. Note that the nanoparticles were uniformly coated on the CFP surface. According to the results of the XRD spectra in Fig. 3, the nanoparticles coated on the surface of CFP were Co_3O_4. As a result, the IPWL irradiation on $Co(NO_3)_2$ with energy densities from 10 to 18 J cm^{-2} creates Co_3O_4 nanoparticles on the CFP substrate. As the energy density further increases to 20 J cm^{-2}, the morphology changes into flake-like nano-structures, as shown in Fig. 4f. The nanoflake structures then gradually grow until the surface of CFP is completely covered with nanoflakes as the energy density further increased to 26 J cm^{-2} (Fig. 4g–i). The size of the nanoflakes decreased after the surface of the CFP was completely covered by nanoflakes, with a further increase in irradiation energy up to 30 J cm^{-2} (Fig. 4j and k). In accordance with the XRD results, the nanoflakes coated on the surface of CFP were cobalt metal. Fig. 4l is a cross-sectional SEM image of the Co nanoflakes on carbon fiber fabricated by IPWL irradiation at an energy density of 30 J cm^{-2}. The Co nanoflakes were uniformly coated on the surface of the carbon fiber, and the thickness of the nanoflake layer was approximately 400–600 nm. Note that all surfaces of the carbon fiber were coated with the Co nanoflakes, even though the IPWL light was irradiated from the right-side of the carbon fiber. The thickness of the cobalt nanoflake layer on the right-side was slightly thicker than that on the left.

The surface area and pore-size distribution of the Co_3O_4 nanoparticles and Co nanoflakes on CFP, which were fabricated at an IPWL energy density of 15 and 30 J cm^{-2}, respectively, were measured using the Brunauer-Emmett-Teller (BET) method. Fig. 5 shows the Ar adsorption-desorption isotherms of the bare CFP, Co_3O_4 nanoparticles, and Co nanoflakes samples, for which the BET surface area values were 0.16, 10.7, and 84.88 m^2 g^{-1}, respectively. The low surface area value of the bare CFP was due to the smooth

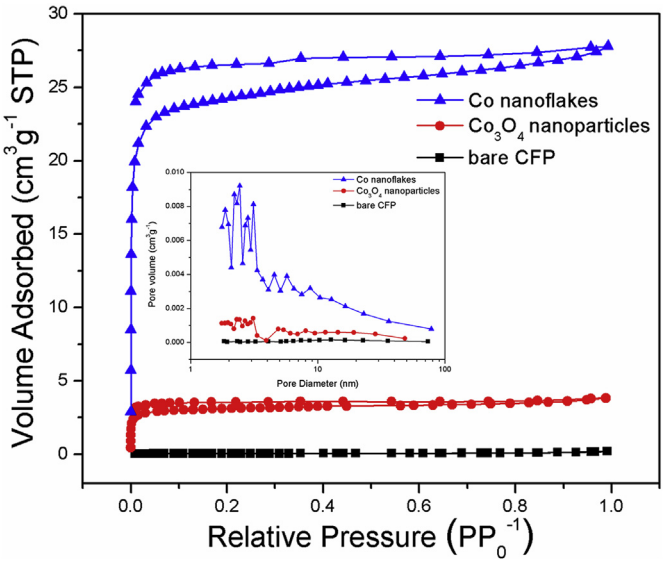

Fig. 5. Ar adsorption-desorption isotherms of the bare CFP, Co_3O_4 nanoparticle/CFP and Co nanoflake/CFP samples. The inset shows their BJH pore-size distribution curves.

surface of the carbon fiber without any pore structures. The adsorption curves of the Co_3O_4 nanoparticles and Co nanoflakes rapidly increased in the very low relative pressure region (>0.1 P P_0^{-1}) and then gradually increased throughout the middle and high relative pressure regions. On the adsorption isotherm plot, the linear increase of Ar uptake in a very low-pressure region indicates monolayer gas adsorption inside the pores, and a near plateau region of adsorption curves at the relative middle- and high-pressure ranges show the presence of micropores with some mesopores. The pore size distributions of the samples calculated using the Barrett-Joyner-Halenda (BJH) method are shown in the inset of Fig. 5. The

BJH adsorption average pore diameters of the Co_3O_4 nanoparticles and Co nanoflakes were 5.2 nm and 4.4 nm, respectively. It is generally known that the highly porous structure and high surface area of the electrode material are favorable for high performance supercapacitors because the ion transfer rate in a porous system and the extent of the electrode/electrolyte interfacial area are determined by the porosity of the electrode material. Therefore, the nanoflake-structured metallic cobalt is expected to exhibit significantly good electrochemical properties.

3.2. Temperature measurements

In order to define the IPWL-assisted photothermal reduction of the cobalt precursor and the synthesis of the cobalt oxide nanoparticles and cobalt nanoflakes, the in-situ temperature of the sample was measured using a lab-made temperature measurement system and analyzed with a transient heat transfer calculation when the IPWL was irradiated on $Co(NO_3)_2$-coated CFP to convert $Co(NO_3)_2$ into cobalt oxide nanoparticles and cobalt nanoflakes. As shown in Fig. 6, the temperature of the silver paste was measured instead of the $Co(NO_3)_2$/CFP because it is difficult to measure the temperature of the $Co(NO_3)_2$/CFP directly due to issues with contact between the CFP and thermocouple. Therefore, the temperature of the sample should be inferred from the analytical solution verified by the experimental results. Fig. 6 represents the experimentally measured temperature and analytical temperature of the Co nanoflake/CFP sample fabricated by 28 J cm^{-2} IPWL irradiation. The experimentally-measured temperature (388.3 °C), which is corresponding to the silver paste temperature of the Co nanoflake/CFP sample fabricated by 28 J cm^{-2} IPWL irradiation, was very close to the analytical results (392.4 °C) from the solution of the transient heat transfer equation (11-a). From the above results and the solution of the transient heat transfer equation (11-b), the temperature of the Co nanoflake/CFP sample is easily calculated as 476.9 °C. The temperatures of the samples at the other IPWL conditions from 10 to 30 J cm^{-2} were inferred from each of the measured temperatures of the silver paste (Table 1). Based on these results, $Co(NO_3)_2$ precursors were subject to thermal effects from the IPWL irradiation rather than direct interaction between the IPWL irradiation and the $Co(NO_3)_2$ precursors. It has been reported that $Co(NO_3)_2$ can be converted to Co_3O_4 at 200 °C, and further reduced to CoO and Co at 260 and 320 °C, respectively, in the presence of H_2/N_2 gas

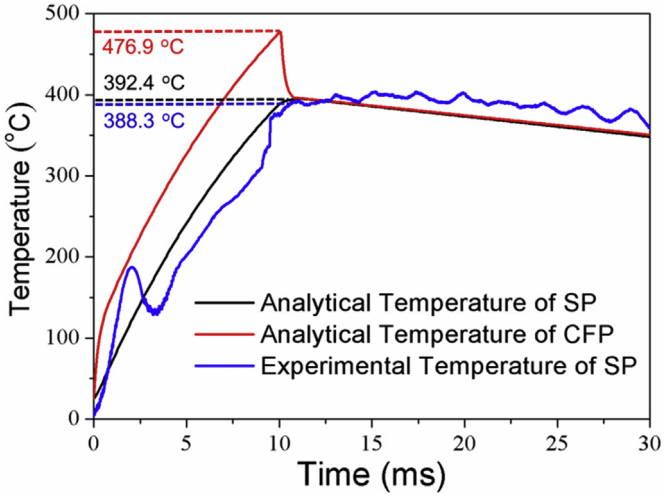

Fig. 6. Analytical temperatures of the CFP and silver paste (SP), and experimental temperature of the SP at 28 J cm^{-2} IPWL irradiation.

according to the following three reactions [40,41]:

$$3Co(NO_3)_2 \rightarrow Co_3O_4 + N_2O_4 + 2N_2O_5 \quad (14)$$

$$Co_3O_4 + H_2 \rightarrow 3CoO + H_2O \quad (15)$$

$$Co_3O_4 + 4H_2 \rightarrow 3Co + 4H_2O \quad (16)$$

As shown in Table 2, $Co(NO_3)_2$/CFP can be heated to 500 °C by IPWL irradiation, which is high enough to convert the cobalt precursor into cobalt oxide and cobalt metal. Note that the fabrication method proposed in this work does not require a vacuum or inert/reducing gas system at any step. Instead, a carbothermal reaction is involved in the proposed reduction process, and the CFP substrate is used as a reducing agent. Carbothermal reduction is a common reduction method for metal oxides and is usually conducted at high temperature in a blast furnace with other carbon materials, such as charcoal. The specific mechanism of carbothermal reduction is not yet proven, but the most widespread mechanism is oxide reduction through gaseous CO and CO_2 intermediates at temperatures below 800–1000 °C [42]. Recently, Y. K. Kim et al. prepared nanoporous cobalt foam by consolidation of a CNT/Co_3O_4 nanocomposite powder at 650 °C for 10 h in an N_2 atmosphere [43]. During heat treatment of this powder in an N_2 atmosphere, Co_3O_4 nanoparticles are reduced to cobalt metal by these possible reactions:

$$Co_3O_4 \rightarrow 3Co + 2O_2 \quad (17)$$

$$2CoO \rightarrow 2Co + O_2 \quad (18)$$

$$C + O_2 \rightarrow CO_2 \quad (19)$$

$$CoO + C \rightarrow Co + CO \quad (20)$$

Compared to this method, the proposed technique in this study is much simpler, faster, and an N_2 atmosphere is not necessary. For the IPWL-induced Co reduction process, the influence of oxygen in the atmosphere may be trivial because IPWL-irradiation can be completed in a few milliseconds to facilitate the reduction of cobalt oxide at a relatively low temperature below 500 °C. Furthermore, the technique proposed in this study does not require strict control over process variables such as pH, temperature, and gas conditions. It is also noteworthy that the entire fabrication procedure, including the processing time for immersion and drying of the precursor on the CFPs followed by IPWL irradiation, is simple and completed in a short time.

Table 2
Temperature, status and shape of Co precursor/CFP with respect to the IPWL irradiation energy.

Energy (J/cm^2)	Temperature (°C)	Status	Shape
10	186.4	Co_3O_4	Nanoparticle
12	218.7	Co_3O_4	Nanoparticle
14	250.9	Co_3O_4	Nanoparticle
16	283.2	Co_3O_4	Nanoparticle
18	315.5	Co_3O_4	Nanoparticle
20	347.8	CoO, Co	Nanoparticle
22	380.0	CoO, Co	Nanoparticle
24	412.3	CoO, Co	Nanoparticle
26	444.6	Co	Nanoflake
28	476.9	Co	Nanoflake
30	509.1	Co	Nanoflake

3.3. Electrochemical characterization

The electrochemical properties of the Co_3O_4 nanoparticle/CFP and Co nanoflake/CFP samples were studied using a three-electrode system for electrochemical energy storage application. The Co_3O_4 nanoparticle/CFP and Co nanoflake/CFP samples were fabricated by IPWL irradiation at energy densities of 15 and 30 J cm^{-2}, respectively. Fig. 7 shows the cyclic voltammetry (CV) curves of bare CFP, Co_3O_4 nanoparticle/CFP, and Co nanoflake/CFP electrodes in 2 M KOH aqueous electrolyte at potential ranges from 0 to 0.6 V with a scan rate of 100 mV s^{-1}. The non-rectangular shape of the CV curves of Co_3O_4 nanoparticle/CFP and Co nanoflake/CFP indicates that non-capacitive faradaic reactions are responsible for charge storage, indicating these materials behave like faradaic battery-type electrode at potential ranges from 0 to +0.6 V [44,45]. Thus, to describe the electrochemical behavior of these battery-type materials, all capacitive values are shown in the form of capacity (mA h) instead of capacitance (F). The charge-storage characteristics of the samples are presented by areal capacity because it is difficult to measure the exact weight of the immersed area of bare CFP. The areal capacity (Q_a) of the electrodes can be obtained via integration of the CV curve using the following equation,

$$Q_a = \frac{\int_{V_i}^{V_f} I(V)dV}{av}, \tag{21}$$

where Q_a is the areal capacity (mA h cm^{-2}), a is the area of the electrodes (cm^2), v is the potential scan rate (V h^{-1}), V_f and V_i are the integration limits of the voltammetric curve (V), and $I(V)$ denotes the response current (mA). The calculated areal capacity for each sample reaches 0.0005, 0.0117, and 0.0267 mAh cm^{-2}. The CV-integrated area of bare CFP was almost negligible compared to other samples, revealing nearly no capacity contribution from the current collector. The areal capacity of the Co nanoflake/CFP electrode is much greater than the Co nanoparticle/CFP electrode.

Fig. 8a shows the CV curves of the Co_3O_4 nanoparticle/CFP electrode in a 2 M KOH aqueous electrolyte at potential ranges from 0 to 0.6 V with various scan rates from 10 to 100 mV s^{-1}. The mass loading of the active materials (Co_3O_4 nanoparticle) is 0.3 mg cm^{-2}. The shape of the curves between 0 and 0.2 V is close to rectangular, indicating contributions from the electric double-layer capacitance. Two pairs of redox peaks due to the faradaic redox reaction at the electrode/electrolyte interface were observed at the potential range from 0.2 to 0.6 V, which indicates that the Co_3O_4 nanoparticle/CFP electrode shows characteristics typical of a battery-type electrode with reversible oxidation and reduction processes. The charge storage mechanism in Co_3O_4 originates from the following redox reactions.

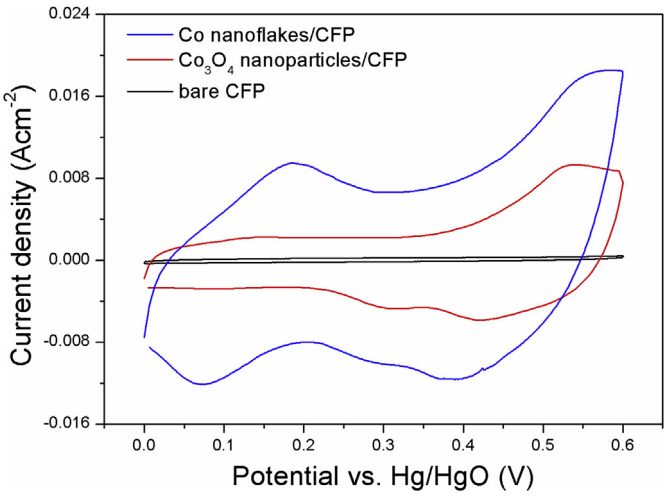

Fig. 7. The cyclic voltammograms of bare CFP, Co_3O_4 nanoparticle/CFP and Co nanoflake/CFP electrodes at a scan rate of 100 mV s^{-1}.

$$Co_3O_4 + OH^- + H_2O \leftrightarrow 3CoOOH + e^- \tag{22}$$

$$CoOOH + OH^- \leftrightarrow CoO_2 + H_2O + e^- \tag{23}$$

In general, the peak separation distance between the oxidation and reduction peaks increases as the scan rate increases because the ion diffusion rate at the electrode-electrolyte interface is comparatively slower than the charge-transfer rate in the electrode at high scan rates because of the resistance of the electrode [46]. As shown in Fig. 8a, the Co_3O_4 nanoparticle/CFP electrode exhibits a slight increase in the peak separation distance, which indicates a low resistance of the electrode. Fig. 8b shows the variation of the specific capacity of the Co_3O_4 nanoparticle/CFP electrode at different scan rates (10–100 mV s^{-1}). The specific capacities were 38, 31, and 29 mA h g^{-1} at scan rates of 10, 50, and 100 mV s^{-1}, respectively. Notably, 77% of the capacity was maintained after the scan rate was increased from 10 to 100 mV s^{-1}, indicating a high rate capability of the electrode. Fig. 8c displays galvanostatic discharge curves of the Co_3O_4 nanoparticle/CFP electrode within the potential range of 0–0.5 V with different current densities from 1 to 10 A g^{-1}. The specific capacity (Q_{sp}) of the electrodes can be calculated from the discharge curves using the following equation:

$$Q_{sp} = \frac{\int Idt}{m}, \tag{24}$$

where I is the discharge current (A), dt represents the discharging time (s) and m is the mass of the active electrode material (g). The specific capacities of 29, 28, 25, and 23 mA h g^{-1} were obtained at current densities of 1, 2, 5, and 10 A g^{-1}. The cycling stability of the Co_3O_4 nanoparticle/CFP electrode was evaluated at a scan rate of 50 mV s^{-1} for 5000 cycles, as shown in Fig. 8d. After 5000 cycles, approximately 88% of the initial specific capacity retention was obtained, which demonstrates excellent cycle stability. The decrease in capacity can be attributed to increased impedance with an increasing number of cycles due to fatigue of the active materials.

Fig. 9 shows the electrochemical analysis of the Co nanoflake/CFP electrode fabricated by 30 J cm^{-2} IPWL irradiation. There are only a few literature references of metallic cobalt based supercapacitors [47,48]. Cobalt and cobalt alloys show excellent corrosion resistance due to the spontaneous formation of a protecting passivation film, and they exhibit an interesting passive behavior in alkaline solutions. It was reported that the electro-oxidation of cobalt in KOH electrolytes occurs at negative potentials in the solid phase and results in the formation of a $Co(OH)_2$ film on a Co electrode [49,50]. $Co(OH)_2$ is further oxidized to Co_3O_4 and CoOOH at more positive potentials. Therefore, the Co nanoflake/CFP electrode can exhibit faradaic charge-storage behavior in the KOH electrolyte. The formation of cobalt hydroxide layer at negative potential in the KOH electrolyte is expressed as follows:

$$Co + 2OH^- \rightarrow Co(OH)_2 + 2e^- \tag{25}$$

Fig. 9a shows CV curves of the Co nanoflake/CFP electrode in the 2 M KOH electrolyte at a potential range from 0 to 0.6 V with various scan rates. The mass loading of the active materials (Co nanoflakes) is 0.3 mg cm^{-2}. Prior to obtaining CV curves, potentiostatic

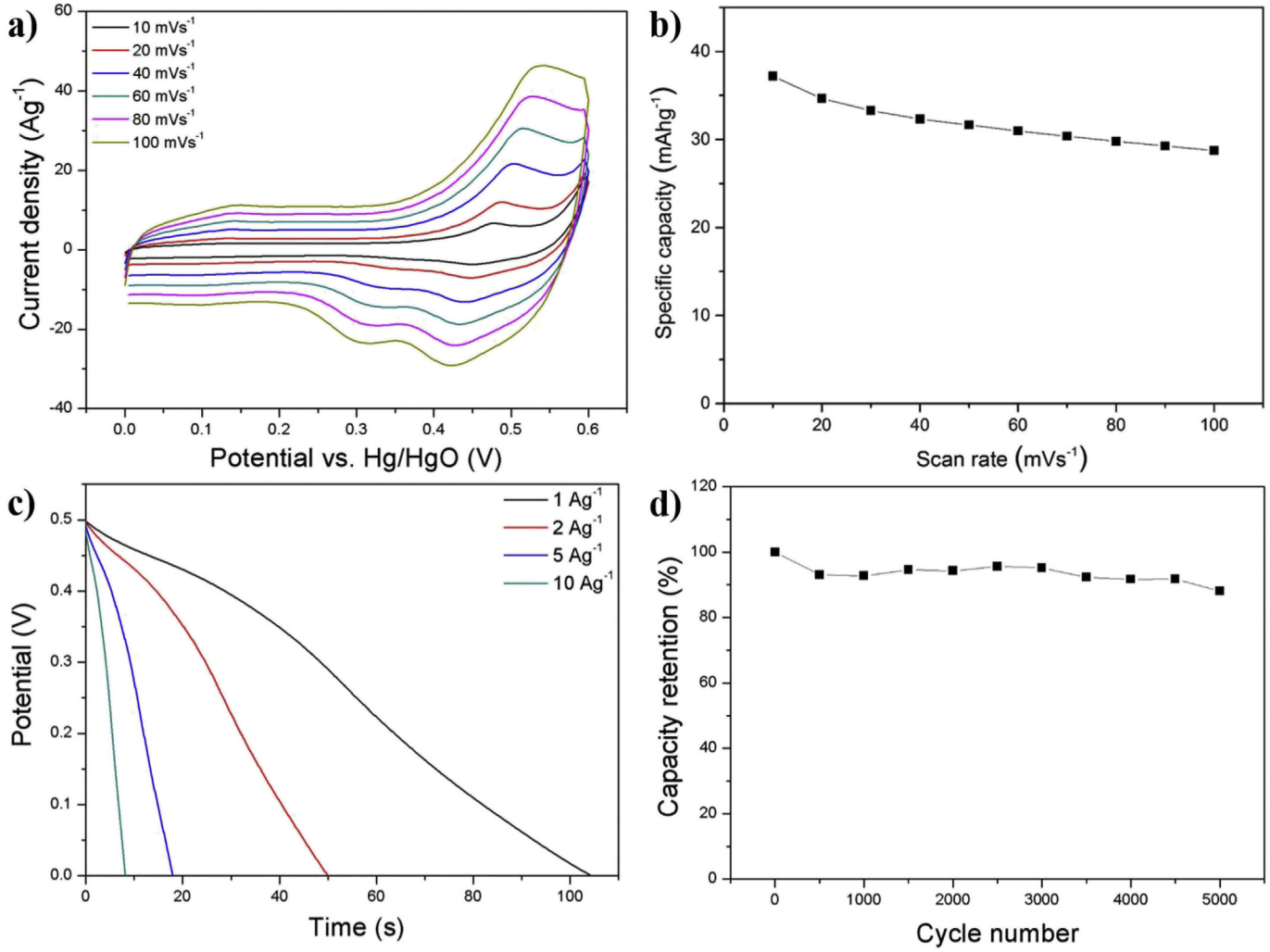

Fig. 8. (a) CV curves of Co_3O_4 nanoparticle/CFP electrode at different scan rates from 10 to 100 mV s^{-1}. (b) Variation of the specific capacity for different scan rates. (c) The discharge curves of Co_3O_4 nanoparticle/CFP electrode at different current densities from 1 to 10 A g^{-1}. (d) Cycling stability of the Co_3O_4 nanoparticle/CFP electrode synthesized with IPWL 15 J cm^{-2}.

oxidation treatment of the Co nanoflake/CFP electrode was performed at a potential of −0.6 V for 5 min to form $Co(OH)_2$ layer on the surface of Co nanoflakes. The CV curves show three pairs of outstanding redox peaks of cobalt oxide and hydroxide due to the following faradaic reactions [49–51]:

$$Co(OH)_2 + OH^- \leftrightarrow CoOOH + H_2O + e^- \quad (26)$$

$$Co_3O_4 + OH^- + H_2O \leftrightarrow 3CoOOH + e^- \quad (27)$$

$$CoOOH + OH^- \leftrightarrow CoO_2 + H_2O + e^- \quad (28)$$

The symmetric characteristic of the redox peaks indicates excellent reversibility of the Co nanoflake/CFP electrode. Furthermore, the shapes of these CV curves show nearly no significant change as the scan rate increases from 10 to 100 mV s^{-1}, implying improved mass transportation, excellent electron conduction within the nanoflakes, and low internal resistance. From the integration of the CV curves, specific capacity values of 70, 53, and 45 mA h g^{-1} were obtained at scan rates of 10, 50, and 100 mV s^{-1}, respectively (Fig. 9b). Fig. 9c shows galvanostatic discharge curves of the Co nanoflake/CFP electrode at potential windows of 0–0.5 V with different current densities, and specific capacities of 73, 67, 55, and 46 mA h g^{-1} were obtained at current densities of 1, 2, 5 and 10 A g^{-1}. The specific capacity of the Co nanoflake/CFP electrode is greater than that of the Co_3O_4 nanoparticle/CFP electrode, which is due to the higher surface area of the Co nanoflakes than the Co_3O_4 nanoparticles. The cycle stability of the Co nanoflake/CFP electrode was also conducted at a scan rate of 50 mV s^{-1} for 5000 cycles. As shown in Fig. 9d, approximately 90% of the initial capacity retention was obtained after 5000 cycles, exhibiting superb long-term stability of the Co nanoflake/CFP electrode. Notably, the specific capacity increases approximately 5% of the initial capacity after 1000 cycles.

Additional experiments were performed to clarify the electrochemical behavior of the electrode materials during stability tests by using XRD and X-ray Photoelectron Spectroscopy (XPS) technique. Fig. 10a presents XRD patterns of the Co nanoflake/CFP electrode before and after the cyclic voltammetry test at a scan rate of 50 mV s^{-1} for 1000 cycles in a 2 M KOH electrolyte. The broad diffraction peak at 26° corresponding to the (111) plane of carbon is due to the CFP substrate. Three distinct diffraction peaks of fcc-cobalt at 44.2, 51.5, and 75.8° appeared for the pristine Co nanoflake/CFP electrode. After 1000 cycles, the intensity of the cobalt metal peaks was reduced to half, and two new peaks appeared at

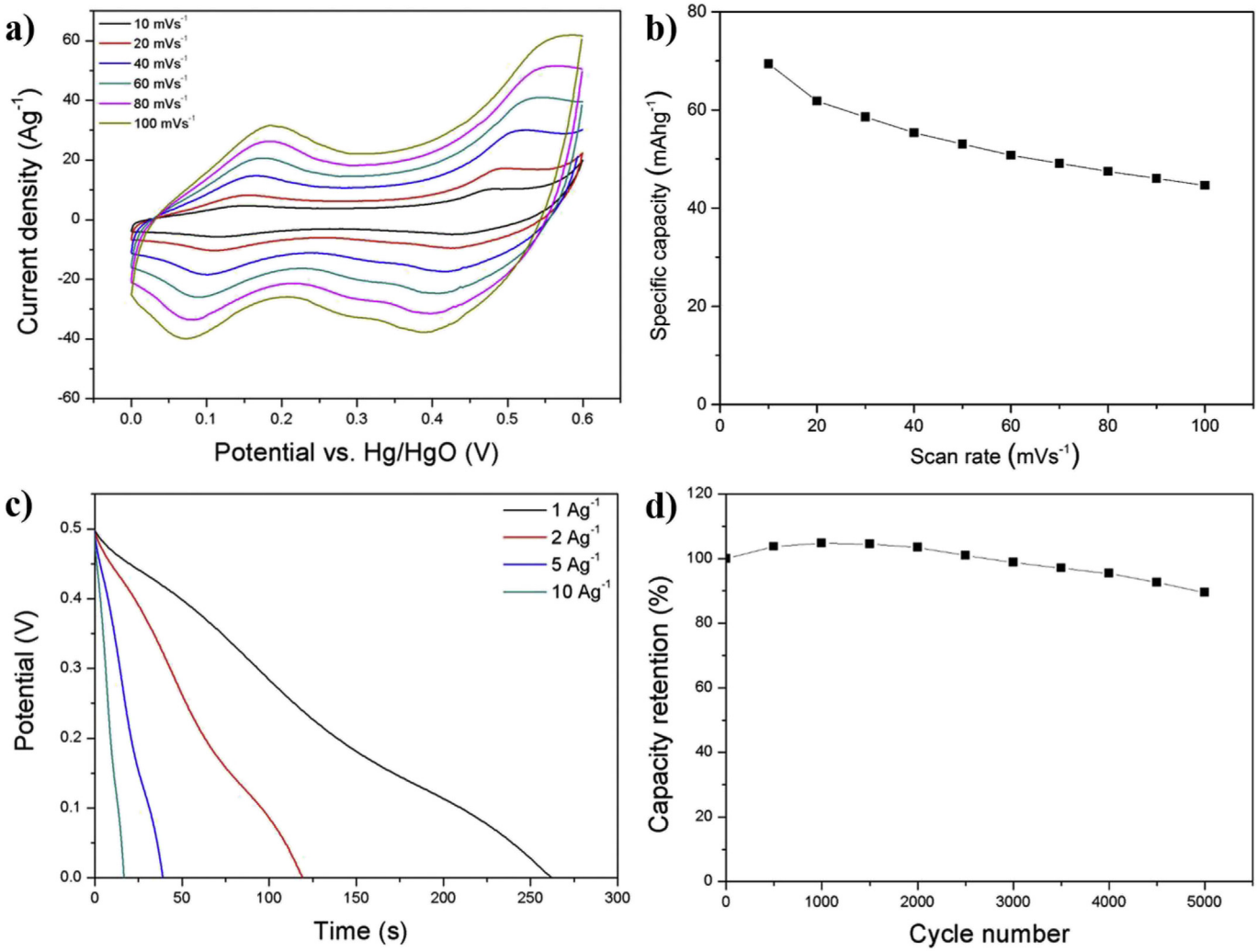

Fig. 9. (a) CV curves of the Co nanoflake/CFP electrode at different scan rates from 10 to 100 mV s^{-1}. (b) Variation of the specific capacity for different scan rates. (c) Discharge curves of the Co nanoflake/CFP electrode at different current densities from 1 to 10 A g^{-1}. (d) Cycling stability of the Co nanoflake/CFP electrode synthesized with IPWL 30 J cm^{-2}.

20.0° and 38.7° that were assignable to the (003) and (012) planes of CoOOH, respectively, with a rhombohedral structure (JCPDS #73-0497), verifying electrochemical oxidation of the cobalt in the KOH electrolyte. Fig. 10b shows the XPS Co 2p spectra of the Co nanoflake/CFP electrode before and after 1000 cycles. The Co nanoflake/CFP electrode shows intense Co $2p_{3/2}$ and Co $2p_{1/2}$ peaks centered at 780.7 and 796.4 eV, respectively attributed to the presence of Co^{2+} [52]. This indicates the existence of CoO at the surface of the cobalt nanoflakes, which probably due to exposure to the laboratory atmosphere. Note that cobalt metal peak is not detected in the spectrum because XPS measures the elemental composition only at the top 1–10 nm of the sample surface. After 1000 cycles, the Co $2p_{3/2}$ peak shifted to 779.7 eV and the distance to the Co $2p_{3/2}$ satellite peak increased from 5.5 eV to 10.1 eV. The Co $2p_{3/2}$ peak at 779.7 eV and the distance of 10.1 eV to the Co $2p_{3/2}$ satellite peak are indicative of the presence of Co^{3+} at the surface [51,53]. Therefore, these results indicate that Co^{2+} at the surface changed to the Co^{3+} state after 1000 cycles. In accordance with the XRD results in Fig. 10a, the Co^{3+} can originate from CoOOH. In alkali solutions, $Co(OH)_2$ undergoes oxidation to CoOOH by the quasi-reversible electrochemical redox reaction [54]. Therefore, the cobalt nanoflakes are gradually oxidized to $Co(OH)_2$ and further oxidized to the CoOOH in KOH electrolyte during the cycle testing, which leads to enhancing the capacity of the Co nanoflake/CFP electrode during the cycles.

4. Conclusion

We demonstrated an ultra-rapid and facile method for the production of well-controlled Co_3O_4 and Co nanostructures on CFP by IPWL photothermal reduction. The mechanism of the IPWL photothermal reduction of cobalt and cobalt oxide was studied by measuring the *in-situ* temperature of the $Co(NO_3)_2$-coated CFP substrate during IPWL irradiation and analyzing the crystal structures of the IPWL-irradiated samples. $Co(NO_3)_2$ was converted to Co_3O_4 nanoparticles by IPWL irradiation with energy densities from 10 to 18 J cm^{-2}, and Co_3O_4 was reduced to CoO and further reduced to Co metal with an increase in energy density. Co nanoflakes were fabricated on the surface of the CFP substrate by irradiation of IPWL with an energy density of 26–30 J cm^{-2}. It was revealed that a carbothermal reaction was involved in the Co reduction process via IPWL irradiation. It is noteworthy that the IPWL-induced carbothermal reduction of metal on the CFP substrate can be conducted under prevalent atmospheric conditions in an extremely short time. The IPWL-induced Co_3O_4 nanoparticle/CFP and Co nanoflake/CFP electrodes exhibited high specific capacities of 29 mA h g^{-1} and

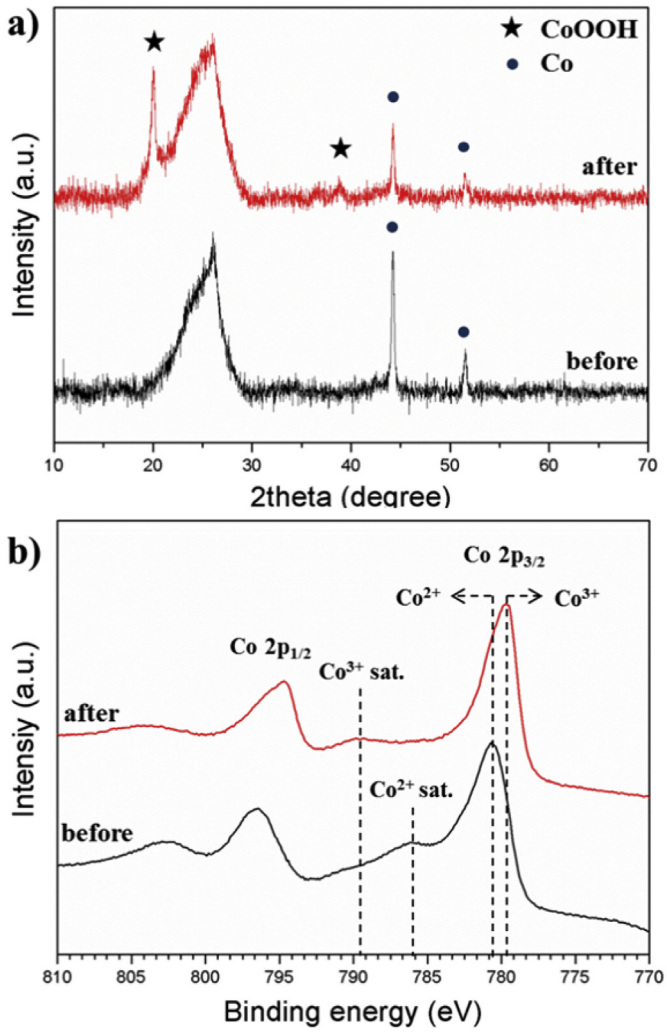

Fig. 10. (a) XRD patterns and (b) XPS Co 2p spectra of the Co nanoflake/CFP electrode before and after 1000 cycles.

73 mA h g^{-1}, respectively, at a current density of 1 A g^{-1} and exhibited excellent rate capability and cycle stability. Note that IPWL-assisted reduction can be readily applied to other metals such as Ni, Cu, Sn, Mn, Fe, and Ag. Therefore, this IPWL photothermal reduction technique has great potential in many fields, including catalysis, energy storage systems, sensors, and filters.

Author contributions

S. Lee and S. H. Park contributed equally to this work.

Acknowledgments

This research was supported by a grant from the Technology Development Program for Strategic Core Materials funded by the Ministry of Trade, Industry and Energy (10047758) and grants from Basic Science Research Program through the National Research Foundation of Korea (NRF) funded by the Ministry of Education (2012R1A6A1029029, 2014M3A7B4052201 and 2015R1A2A2A01008398), Republic of Korea.

References

[1] W. Betteridge, The properties of metallic cobalt, Prog. Mater. Sci. 24 (1979) 51–142.
[2] F.C. Campbell, Elements of Metallurgy and Engineering Alloys, ASM International, Ohio, 2008.
[3] S. Luo, K. Wang, J. Wang, K. Jiang, Q. Li, S. Fan, Binder-free $LiCoO_2$/carbon nanotube cathodes for high-performance lithium ion batteries, Adv. Mater. 24 (2012) 2294–2298.
[4] R.R. Salunkhe, K. Jang, S.-w. Lee, H. Ahn, Aligned nickel-cobalt hydroxide nanorod arrays for electrochemical pseudocapacitor applications, RSC Adv. 2 (2012) 3190–3193.
[5] R.R. Salunkhe, K. Jang, S.-w. Lee, S. Yu, H. Ahn, Binary metal hydroxide nanorods and multi-walled carbon nanotube composites for electrochemical energy storage applications, J. Mater. Chem. 22 (2012) 21365–21630.
[6] J. Jablonski, High temperature reduction with hydrogen, phase composition, and activity of cobalt/silica catalysts, J. Catal. 220 (2003) 146–160.
[7] B. Warne, O.I. Kasyutich, E.L. Mayes, J.A.L. Wiggins, K.K.W. Wong, Self-assembled nanoparticulate Co:Pt for data storage applications, IEEE Trans. Magn. 36 (2000) 3009–3011.
[8] D. Jonynaite, J. Senvaitiene, A. Beganskiene, A. Kareiva, Spectroscopic analysis of blue cobalt smalt pigment, Vib. Spectrosc. 52 (2010) 158–162.
[9] S.-H. Chang, S.-L. Chen, Characterization and properties of sintered WC–Co and WC–Ni–Fe hard metal alloys, J. Alloys Compd. 585 (2014) 407–413.
[10] A.F. Holleman, E. Wiberg, N. Wiberg, Cobalt, in Lehrbuch der Anorganischen Chemie, 102nd ed, de Gruyter, Berlin, 2007, pp. 1146–1152.
[11] R.N. Grass, W.J. Stark, Gas phase synthesis of fcc-cobalt nanoparticles, J. Mater. Chem. 16 (2006) 1825–3108.
[12] R.J. Joseyphus, T. Matsumoto, H. Takahashi, D. Kodama, K. Tohji, B. Jeyadevan, Designed synthesis of cobalt and its alloys by polyol process, J. Solid State Chem. 180 (2007) 3008–3018.
[13] M. Salavati-Niasari, F. Davar, M. Mazaheri, M. Shaterian, Preparation of cobalt nanoparticles from [bis(salicylidene)cobalt(II)]–oleylamine complex by thermal decomposition, J. Magn. Magn. Mater. 320 (2008) 575–578.
[14] Y.L. Hou, H. Kondoh, T. Ohta, Self-assembly of Co nanoplatelets into spheres: synthesis and characterization, Chem. Mater. 17 (2005) 3994–3996.
[15] G. Seong, S. Takami, T. Arita, K. Minami, D. Hojo, A.R. Yavari, T. Adschiri, Supercritical hydrothermal synthesis of metallic cobalt nanoparticles and its thermodynamic analysis, J. Supercrit. Fluids 60 (2011) 113–120.
[16] X. Xi, Z. Nie, Y. Jiang, X. Xu, T. Zuo, Preparation and characterization of ultrafine cobalt powders and supported cobalt catalysts by freeze-drying, Powder Technol. 191 (2009) 107–110.
[17] H.-Y. Lin, Y.-W. Chen, The mechanism of reduction of cobalt by hydrogen, Mater. Chem. Phys. 85 (2004) 171–175.
[18] V.F. Puntes, P. Gorostiza, D.M. Aruguete, N.G. Bastus, A.P. Alivisatos, Collective behaviour in two-dimensional cobalt nanoparticle assemblies observed by magnetic force microscopy, Nat. Mater. 3 (2005) 263–268.
[19] S. Zola, R.U. Ribeiro, J.M.C. Bueno, D. Zanchet, P.A. Arroyo, Cobalt nanoparticles prepared by three different methods, J. Exp. Nanosci. 9 (2012) 398–405.
[20] S. Lentijo-Mozo, R.P. Tan, C. Garcia-Marcelot, T. Altantzis, P.F. Fazzini, T. Hungria, B. Cormary, J.R. Gallagher, J.T. Miller, H. Martinez, S. Schrittwieser, J. Schotter, M. Respaud, S. Bals, G. Van Tendeloo, C. Gatel, K. Soulantica, Air- and water-resistant noble metal coated ferromagnetic cobalt nanorods, ACS Nano 9 (2015) 2792–2804.
[21] G. Ji, Z. Gong, Y. Liu, X. Chang, Y. Du, M. Qamar, Fabrication and magnetic properties of cobalt nanorod arrays containing a number of ultrafine nanowires electrodeposited within an AAO/SBA-15 template, Solid State Commun. 151 (2011) 1151–1155.
[22] S.-i. Kim, H. Yoon, H. Lee, S. Lee, Y. Jo, S. Lee, J. Choo, B. Kim, Epitaxy-driven vertical growth of single-crystalline cobalt nanowire arrays by chemical vapor deposition, J. Mater. Chem. C 3 (2015) 100–106.
[23] K. Gandha, K. Elkins, N. Poudyal, X. Liu, J.P. Liu, High energy product developed from cobalt nanowires, Sci. Rep. 4 (2014) 5345.
[24] M. Comesaña-Hermo, D. Ciuculescu, Z.-A. Li, S. Stienen, M. Spasova, M. Farle, C. Amiens, Stable single domain Co nanodisks: synthesis, structure and magnetism, J. Mater. Chem. 22 (2012) 8043–8047.
[25] V.F. Puntes, D. Zanchet, C.K. Erdonmez, A.P. Alivisatos, Synthesis of hcp-Co nanodisks, J. Am. Chem. Soc. 124 (2002) 12874–12880.
[26] H. Wang, C. Chen, Y. Zhang, L. Peng, S. Ma, T. Yang, H. Guo, Z. Zhang, D.S. Su, J. Zhang, In situ oxidation of carbon-encapsulated cobalt nanocapsules creates highly active cobalt oxide catalysts for hydrocarbon combustion, Nat. Commun. 6 (2015) 7181.
[27] Z.H. Wang, C.J. Choi, B.K. Kim, J.C. Kim, Z.D. Zhang, Characterization and magnetic properties of carbon-coated cobalt nanocapsules synthesized by the chemical vapor-condensation process, Carbon 41 (2003) 1751–1758.
[28] Q. Xie, Z. Dai, W. Huang, J. Liang, C. Jiang, Y. Qian, Synthesis of ferromagnetic single-crystalline cobalt nanobelts via a surfactant-assisted hydrothermal reduction process, Nanotechnology 16 (2005) 2958–2962.
[29] K. Srivastava, S. Madhavi, T.J. White, R.V. Ramanujan, Template assisted assembly of cobalt nanobowl arrays, J. Mater. Chem. 15 (2005) 4424–4428.
[30] Y.J. Zhang, Q. Yao, Y. Zhang, T.Y. Cui, D. Li, W. Liu, W. Lawrence, Z.D. Zhang, Solvothermal synthesis of magnetic chains self-assembled by flowerlike cobalt submicrospheres, Cryst. Growth Des. 8 (2008) 3206–3212.
[31] Y. Zhu, Q. Yang, H. Zheng, W. Yu, Y. Qian, Flower-like cobalt nanocrystals by a complex precursor reaction route, Mater. Chem. Phys. 91 (2005) 293–297.
[32] X. Yang, Q.-w. Chen, J.-z. Zhang, Shape-controlled synthesis and self-assembly of hexagonal cobalt ultrathin nanoflakes, Mater. Chem. Phys. 113 (2009) 675–679.

[33] S. Senapati, S.K. Srivastava, S.B. Singh, Synthesis, magnetic properties and catalytic activity of hierarchical cobalt microflowers, J. Nanosci. Nanotechnol. 12 (2012) 3048–3058.
[34] H.A. Colorado, S.R. Dhage, J.M. Yang, H.T. Hahn, in: TMS, Supplemental Proceedings: Materials Processing and Interfaces, vol. 1, John Wiley & Sons, New Jersey, 2012, pp. 577–584.
[35] J. Ryu, H.-S. Kim, H.T. Hahn, Reactive sintering of copper nanoparticles using Intense pulsed light for printed electronics, J. Electron. Mater. 40 (2010) 42–50.
[36] R. Dharmadasa, M. Jha, D.A. Amos, T. Druffel, Room temperature synthesis of a copper ink for the intense pulsed light sintering of conductive copper films, ACS Appl. Mater. Interfaces 5 (2013) 13227–13234.
[37] E.B. Secor, B.Y. Ahn, T.Z. Gao, J.A. Lewis, M.C. Hersam, Rapid and versatile photonic annealing of graphene inks for flexible printed electronics, Adv. Mater. 27 (2015) 6683–6688.
[38] S.-H. Park, W.-H. Chung, H.-S. Kim, Temperature changes of copper nanoparticle ink during flash light sintering, J. Mater. Process. Technol. 214 (2014) 2730–2738.
[39] B.W. Lee, R. Alsenz, A. Ignatiev, M.A. Van Hove, Surface structures of the two allotropic phases of cobalt, Phys. Rev. B 17 (1978) 1510–1520.
[40] C. Ehrhardt, M. Gjikaj, W. Brockner, Thermal decomposition of cobalt nitrato compounds: preparation of anhydrous cobalt(II) nitrate and its characterization by Infrared and Raman spectra, Thermochim. Acta 432 (2005) 36–40.
[41] H.K. Lin, H.C. Chiu, H.C. Tsai, S.H. Chien, C.B. Wang, Synthesis, characterization and catalytic oxidation of carbon monoxide over cobalt oxide, Catal. Lett. 88 (2003) 169–174.
[42] B.V. L'vov, Mechanism of carbothermal reduction of iron, cobalt, nickel and copper oxides, Thermochim. Acta 360 (2000) 109–120.
[43] T. Brousse, D. Belanger, J.W. Long, To be or not to be pseudocapacitive? J. Electrochem, Soc. 162 (2015) A5185–A5189.
[44] L. Guan, L. Yu, G.Z. Chen, Capacitive and non-capacitive faradaic charge storage, Electrochim. Acta 206 (2016) 464–478.
[45] Y.K. Kim, S.I. Cha, S.H. Hong, Nanoporous cobalt foam and a $Co/Co(OH)_2$ core–shell structure for electrochemical applications, J. Mater. Chem. A 1 (2013) 9802–9808.
[46] G. Wang, L. Zhang, J. Zhang, A review of electrode materials for electrochemical supercapacitors, Chem. Soc. Rev. 41 (2012) 797–828.
[47] L. Wang, D. Wang, X. Hu, J. Zhu, X. Liang, Preparation of metallic cobalt-graphene composites with enhanced electrochemical activity, Electrochim. Acta 76 (2012) 282–287.
[48] F. Wei, J. Jiang, G. Yu, Y. Sui, A novel cobalt-carbon composite for the electrochemical supercapacitor electrode material, Mater. Lett. 146 (2015) 20–22.
[49] W.K. Behl, J.E. Toni, Anodic oxidation of cobalt in potassium hydroxide electrolytes, J. Electroanal. Chem. Interfacial Electrochem 31 (1971) 63–75.
[50] K.M. Ismail, W.A. Badawy, Electrochemical and XPS investigations of cobalt in KOH solutions, J. Appl. Electrochem 30 (2000) 1303–1311.
[51] A. Foelske, H.-H. Strehblow, Structure and composition of electrochemically prepared oxide layers on Co in alkaline solutions studied by XPS, Surf. Interface Anal. 34 (2002) 125–129.
[52] C.D. Wagner, W.M. Riggs, L.E. Davis, J.F. Moulder, G.E. Mullenberg, Handbook of X-ray Photoelectron Spectroscopy, Perkin-Elmer, Minnesota, 1979.
[53] P. Vialat, C. Mousty, C. Taviot-Gueho, G. Renaudin, H. Martinez, J.-C. Dupin, E. Elkaim, F. Leroux, High-performing monometallic cobalt layered double hydroxide supercapacitor with defined local structure, Adv. Func. Mater. 24 (2014) 4831–4842.
[54] P. Elumalai, H.N. Vasan, N. Munichandraiah, Electrochemical studies of cobalt hydroxide - an additive for nickel electrodes, J. Power Sources 93 (2001) 201–208.